

Differential correction and arc-length continuation applied to boundary value problems: examples based on snap-through of circular arches and spherical shells

Jun Zhong^{a,*}, Shane D. Ross^b

^a*Engineering Mechanics Program
Virginia Tech
Blacksburg, VA 24061, USA*

^b*Department of Aerospace and Ocean Engineering
Virginia Tech
Blacksburg, VA 24061, USA*

Abstract

Inspired by the application of differential correction to initial-value problems to find periodic orbits in both the autonomous and non-autonomous dynamical systems, in this paper we apply differential correction to boundary-value problems. In the numerical demonstration, the snap-through buckling of arches and shallow spherical shells in structural mechanics are selected as examples. Due to the complicated geometrical nonlinearity in such problems, the limit points and turning points might exist. In this case, the typical Newton-Raphson method commonly used in numerical algorithms will fail to cross such points. In the current study, an arc-length continuation is introduced to enable the current algorithm to capture the complicated load-deflection paths. To show the accuracy and efficiency of differential correction, we will also apply the continuation software package COCO to get the results as a comparison to those from differential correction. The results obtained by the proposed algorithm and COCO agree well with each other, suggesting the validity and robustness of differential correction for boundary-value problems.

Keywords:

Differential correction, Arc-length continuation, Boundary-value problems, Snap-through, Arches and spherical shells

*Corresponding author: junzhong@vt.edu (J. Zhong)

1. Introduction

Nonlinear behaviors can be widely found in both the natural world and engineering applications. In general, however, it is difficult to get the analytical solutions for nonlinear systems. The increase of degrees of freedom makes it even harder. In order to efficiently find more accurate solutions for nonlinear systems, researchers have kept attempting to develop new numerical algorithms, such as the finite element method (FEM) [1], the differential quadrature method (DQM) [2], the mesh-free method [3], to name but a few. Generally, when applying the numerical algorithm the discretization process is needed by meshing the domain into small elements (e.g., in FEM) or using an appropriate number of sampling points (e.g., in DQM and the mesh-free method). After the discretization, the nonlinear differential equations are converted to nonlinear algebraic equations which need to be solved by an iteration process.

Differential correction [4–8], or simply the shooting method [9], is a widely used numerical method in the analysis of finite-dimensional continuous dynamical systems. One common application is to obtain the periodic orbits in both the autonomous systems [10–12] and non-autonomous systems [13, 14]. It uses the state transition matrix, the solution to the variational equations of the governing ordinary differential equations, to measure the linear relationship between the perturbation of the initial conditions and the final displacements of a specific reference trajectory. The initial conditions are adjusted according to the state transition matrix by iteration so that the final displacements can be searched to target the desired final state. For periodic orbits, the trajectory will return to its original state after one period so that the goal is to correct the initial condition to realize the coincidence of initial and final states. The difference between autonomous and non-autonomous systems (by which we mean time-periodic systems) is that the period of periodic orbits for the former case is unknown, while in the later case it is equal to an integer multiple of the external excitation.

Different from other numerical methods, differential correction does not need any discretization process so that it will not yield a large matrix even when the dimension of the system increases. Any integration algorithm for solving the initial-value problem can work, such as the Runge-Kutta [9] or Newmark method [15]. Considering this advantage, we seek to extend the application of differential correction to the boundary-value problems. In this case, we need to regard the boundary-value problems as initial value problems by considering the boundary conditions at one end as the initial conditions which need to be adjusted to satisfy the boundary conditions at the other end.

Generally when dealing with nonlinear problems by numerical algorithms, an iteration process is necessary after the discretization among which the Newton-Raphson method is a popular one due to its rapid convergence. It keeps parameters constant during the iteration process, such as the external load applied to plates and shells. However, it requires a good initial guess to guarantee the convergence. Moreover, problems will appear when the iteration process is faced with a limit point (the local minimum or maximum of the equilibrium path, such as points A, B, D, and G as shown in Figure 1) or a turning point (snap-back point, such as points E and F). For example, curved structures which have multistability can withstand a certain loading. When subjected to large external loading or sufficient disturbance, the structures will snap-through to a remote equilibrium state. This behavior is sudden and associated with a fast dynamic jump which presents

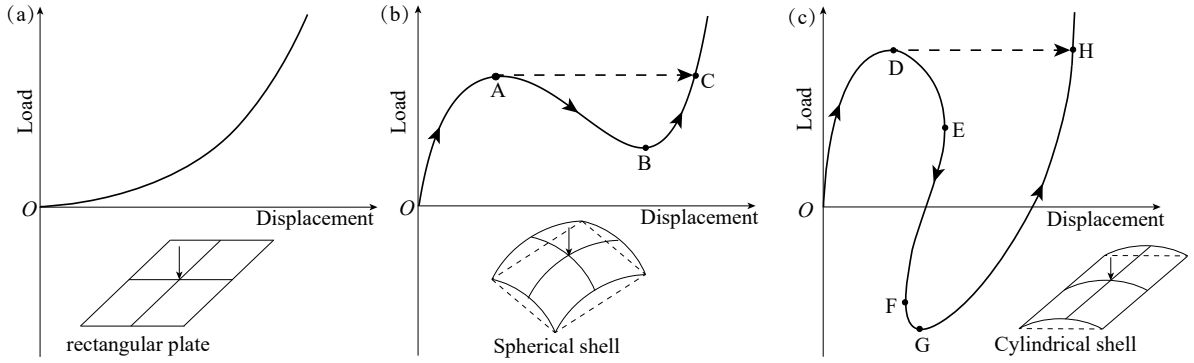


Figure 1: A qualitative schematic of the load-displacement relation of a plate, a spherical shell, and a cylindrical shell. The three structures have the same dimensions, loading and boundary conditions, but different initial curvatures. Of course, the change of parameters for the shells might topologically change the equilibrium paths. The corresponding quantitative study of such structures is given in [16]. Readers are referred to the paper for details. (a) shows the classic nonlinear bending of a rectangular plate whose load-displacement relation present a monotonic behavior which can be captured by the classic Newton-Raphson method under either load-control or displacement-control. (b) gives the classic snap-through of a spherical shell. The Newton-Raphson method with load-control will fail to capture the whole path. Once the limit point C on the equilibrium path is reached, a slight increase of load will trigger a quick snap-through into its inverted position C without capturing curve A-B-C. However, the whole path can be traced by displacement-control. (c) shows a more complicated snap-through of a cylindrical shell. Different from the previous two examples, the complexity of the current structure comes from the existence of turning points E and F. The typical Newton-Raphson method fails in capturing the whole load-displacement curve.

a decrease in the load along the equilibrium path [17, 18]. The Newton-Raphson method fails in capturing the branch after the limit point, such as A-B-C in Figure 1(b) and D-E-F-G-H in Figure 1(c). Although some strategies, such as using the displacement as the increment parameter, were developed to cross the limit points, they still fail when the snap-back phenomena appear [19], such as points E and F in Figure 1(c). To allow numerical continuation safely past the limit point, Risks [20] creatively developed a pseudo arc-length method. It seeks a new equilibrium point along the normal direction of the tangent to the current or known equilibrium state at a prescribed distance along the tangent. Later, other types of arc-length methods were created [19]. To make the current algorithm capable of passing the limit points and turning points so that the complicated equilibrium path can be detected, the arc-length continuation will be adopted.

In this paper, we apply differential correction to boundary-value problems using the snap-through of arches and spherical shells as examples to show the current algorithm. Since the limit points might exist in these systems, an arc-length method will be used as the continuation tool. In order to compare the effectiveness and robustness of differential correction to the state of the art, the software package COCO [21] is also used. In Section 2, we give a detailed derivation of differential correction and the arc-length continuation. In Section 3, mathematical models of the arches and shallow spherical caps are introduced, followed by numerical results and discussions.

2. Numerical method

2.1. Differential correction method

As discussed in the introduction, differential correction or shooting method is commonly used to find the periodic orbits in both the autonomous and non-autonomous systems [10–14]. The idea is to properly select the approximations as the initial seeds and update the initial conditions in an iterative process so that the final state returns to the initial state. In this paper, we aim to extend the application of differential correction from initial-value problems to boundary value problems, using structural mechanics as examples. In practical applications, limit points or turning points are frequently encountered. To make the current algorithm more versatile, the arc-length continuation will be embedded.

In what follows, we briefly describe the idea of differential correction. When applying differential correction, the boundary-value problem will be regarded as an initial-value problem. The boundary conditions at one boundary should be considered as initial conditions which will be modified by differential correction until the boundary conditions at the other boundary of the domain are satisfied by which the system is solved.

Consider a continuous, autonomous, dynamical system of the form,

$$\frac{du}{dt} = f(u, \lambda, t), \quad \text{where } u \in \mathbb{R}^n, \quad \lambda \in \mathbb{R}^p, \quad (1)$$

where $t \in \mathbb{R}$ is the independent variable, u is the (dependent) n -dimensional *state variable*, λ is a set of p *parameters*, and the *flow field* f is an n -dimensional \mathbf{C}^r vector field with respect to u and λ . We will limit our discussion to the case of $p = 1$ parameter so that the functional dependence of f is,

$$f : \mathbb{R}^n \times \mathbb{R} \rightarrow \mathbb{R}^n, \quad (u, \lambda) \mapsto f(u, \lambda).$$

Let the trajectories of the system (1) with initial condition $u(t_0) = u_0$ and parameter $\lambda = \lambda_0$ be denoted by the *flow map* $\phi(t, t_0; u_0, \lambda_0)$ or simply¹ $\phi(t; u_0, \lambda_0)$, with dependence,

$$\phi : \mathbb{R} \times \mathbb{R}^n \times \mathbb{R} \rightarrow \mathbb{R}^n, \quad (t, u_0, \lambda_0) \mapsto \phi(t; u_0, \lambda_0).$$

One can easily verify the flow map satisfies the dynamical system (1),

$$\frac{d}{dt} \phi(t; u_0, \lambda_0) = f(\phi(t; u_0, \lambda_0), \lambda_0), \quad \text{with initial condition } \phi(t_0; u_0, \lambda_0) = u_0. \quad (2)$$

For a specific time t_1 , we denote $u_1 = \phi(t_1; u_0, \lambda_0)$. A schematic of the flow map is shown in Figure 2.

Consider a *reference trajectory* $\bar{u}(t)$ with initial condition \bar{u}_0 at time t_0 and parameter $\bar{\lambda}_0$. Also select a nearby trajectory with a displaced initial condition $\bar{u}_0 + \delta\bar{u}_0$ and perturbed parameter $\bar{\lambda}_0 + \delta\bar{\lambda}_0$, that is, it starts out with the state and parameter displaced by $\delta\bar{u}_0$ and $\delta\bar{\lambda}_0$, respectively, from that of the reference trajectory. The perturbation of the state

¹Since the flow map of an autonomous ordinary differential equation does not depend on the initial time t_0 , but only the elapsed time $t - t_0$.

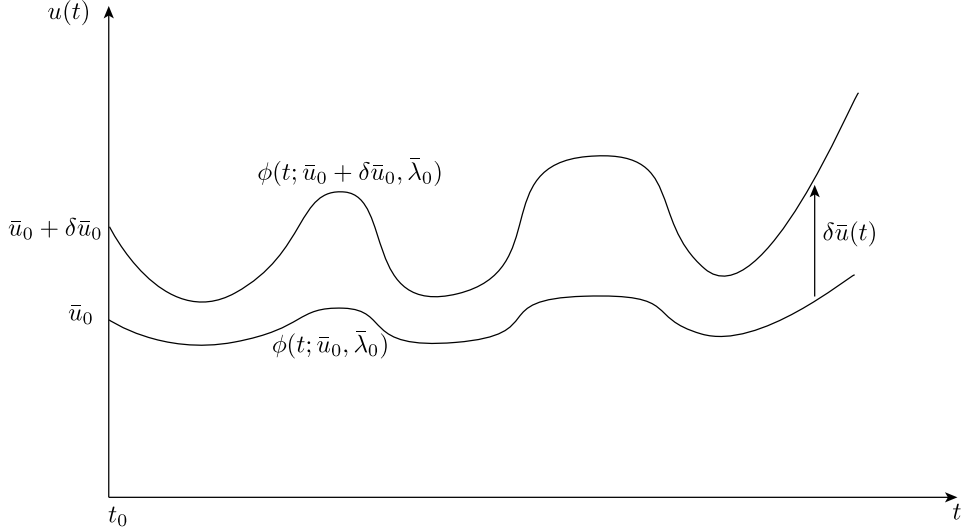


Figure 2: A schematic of the flow map. We show the reference trajectory $\phi(t; \bar{u}_0, \bar{\lambda}_0)$ and a neighboring trajectory $\phi(t; \bar{u}_0 + \delta \bar{u}_0, \bar{\lambda}_0)$ starting from an initial condition displaced by $\delta \bar{u}_0$ from the reference initial condition. No perturbation of $\bar{\lambda}_0$ is considered for simplicity.

will evolve as the n -dimensional vector displacement of the perturbed trajectory from the reference trajectory,

$$\delta \bar{u}(t; \bar{\lambda}_0 + \delta \bar{\lambda}_0) = \phi(t; \bar{u}_0 + \delta \bar{u}_0, \bar{\lambda}_0 + \delta \bar{\lambda}_0) - \phi(t; \bar{u}_0, \bar{\lambda}_0). \quad (3)$$

Measuring the displacement at time t_1 and expanding in a Taylor series in $\delta \bar{u}_0$ and $\delta \bar{\lambda}_0$ yields,

$$\delta \bar{u}(t_1; \bar{\lambda}_0 + \delta \bar{\lambda}_0) = \frac{\partial \phi(t_1; \bar{u}_0, \bar{\lambda}_0)}{\partial u_0} \delta \bar{u}_0 + \frac{\partial \phi(t_1; \bar{u}_0, \bar{\lambda}_0)}{\partial \lambda_0} \delta \bar{\lambda}_0 + \text{higher order terms in } \delta \bar{u}_0 \text{ and } \delta \bar{\lambda}_0. \quad (4)$$

Note that in initial-value problems, t_0 and t_1 are often considered the initial and final *time*, while in the boundary-value problem context considered here, they are the two *boundaries*. The $n \times n$ matrix, $\frac{\partial \phi(t_1; \bar{u}_0, \bar{\lambda}_0)}{\partial u_0}$, which satisfies the above relation to first-order, when $\delta \bar{\lambda}_0 = 0$, is called the *state transition matrix*, usually denoted by $\Phi(t_1, t_0; \bar{\lambda}_0)$. It measures the initial and final displacements by the linear relationship

$$\delta \bar{u}(t_1; \bar{\lambda}_0) = \Phi(t_1, t_0; \bar{\lambda}_0) \delta \bar{u}_0, \quad (5)$$

when there is no perturbation on the parameter. It can be obtained as the fundamental matrix solution to the linear *variational equations* of (1),

$$\delta \dot{\bar{u}}(t; \bar{\lambda}_0) = Df(\bar{u}(t), \bar{\lambda}_0) \delta \bar{u}, \quad (6)$$

which are the linearized equations for the evolution of the ‘variations’, that is, displacements, $\delta\bar{u}$ about the reference trajectory $\bar{u}(t)$. Here $Df(\bar{u}(t), \bar{\lambda}_0) = \frac{\partial f}{\partial u}(\bar{u}(t), \bar{\lambda}_0)$ is the Jacobian matrix of the flow field f evaluated along the reference trajectory $\bar{u}(t)$ when there is no perturbation on the parameter.

The n -dimensional vector $\frac{\partial\phi(t_1, \bar{u}_0, \bar{\lambda}_0)}{\partial\lambda_0}$ in (4), denoted by $\Phi_\lambda(t_1, t_0; \bar{\lambda}_0)$, measures the sensitivity of the final displacement with respect to the perturbation of the parameter, $\delta\bar{\lambda}_0$, that is,

$$\delta\bar{u}(t_1; \bar{\lambda}_0) = \Phi(t_1, t_0; \bar{\lambda}_0)\delta\bar{\lambda}_0, \quad (7)$$

when there is no initial displacement, i.e., when $\delta\bar{u}_0 = 0$.

Computation of Φ and Φ_λ . To apply the differential correction procedure, one needs to compute the state transition matrix Φ and the vector Φ_λ along a reference trajectory. Since the flow map $\phi(t; \bar{u}_0, \bar{\lambda}_0)$ satisfies (2), we differentiate this equation with respect to the initial condition u_0 and obtain,

$$\frac{d}{dt} \frac{\partial\phi(t; \bar{u}_0, \bar{\lambda}_0)}{\partial u_0} = Df(\phi) \frac{\partial\phi(t; \bar{u}_0, \bar{\lambda}_0)}{\partial u_0}, \quad \text{with} \quad \frac{\partial\phi(t_0; \bar{u}_0, \bar{\lambda}_0)}{\partial u_0} = I_n, \quad (8)$$

where I_n is the $n \times n$ identity matrix. Hence, the state transition matrix Φ solves the following initial value problem,

$$\dot{\Phi}(t, t_0; \bar{\lambda}_0) = Df(\bar{u}(t))\Phi(t, t_0; \bar{\lambda}_0), \quad \text{with initial condition, } \Phi(t_0, t_0; \bar{\lambda}_0) = I_n. \quad (9)$$

On the other hand, since the flow map $\phi(t; \bar{u}_0, \bar{\lambda}_0)$ also depends on the parameter $\bar{\lambda}_0$, we differentiate (2) with respect to λ_0 and obtain,

$$\frac{d}{dt} \frac{\partial\phi(t; \bar{u}_0, \bar{\lambda}_0)}{\partial\lambda_0} = Df(\phi) \frac{\partial\phi(t; \bar{u}_0, \bar{\lambda}_0)}{\partial\lambda_0} + \frac{\partial f}{\partial\lambda_0}, \quad \text{with} \quad \frac{\partial\phi(t_0; \bar{u}_0, \bar{\lambda}_0)}{\partial\lambda_0} = 0, \quad (10)$$

Denoting $f_\lambda = \frac{\partial f(t; \bar{u}_0, \bar{\lambda}_0)}{\partial\lambda_0}$ and using Φ_λ from before, this can be rewritten as another initial value problem,

$$\dot{\Phi}_\lambda(t, t_0; \bar{\lambda}_0) = Df(\bar{u}(t))\Phi_\lambda(t, t_0; \bar{\lambda}_0) + f_\lambda, \quad \text{with initial condition, } \Phi_\lambda(t_0, t_0; \lambda_0) = 0. \quad (11)$$

Note that generally (1), and more specifically the flow map (2), cannot be solved analytically, which means (9) and (11) are also not available analytically. In this case, we need to simultaneously solve, via numerical integration, $n^2 + 2n$ first-order scalar differential equations in (9), (11), and (2), representing the elements of Φ , Φ_λ , and ϕ , associated with the dynamical system (1).

Arc-length method. Once we numerically integrate (2), (9) and (11), we obtain the final states of the system so that we can use the differential correction procedure to adjust the initial conditions in order to target the desired final states. In a general case where a limit point (the local maximum or minimum) exists, Newton-Raphson type continuation methods which usually fix the load parameter will fail. In order to pass such points, we will introduce arc-length continuation to find the equilibrium path which allows for variable parameters.

Suppose we want to satisfy a specific state at time t_1 (or specific boundary conditions in boundary-value problems) such that,

$$R(\bar{u}_0, \bar{u}_1, \bar{\lambda}_0) = 0, \quad (12)$$

where for now we let the form of R be general, merely assuming the functional form

$$R : \mathbb{R}^n \times \mathbb{R}^n \times \mathbb{R} \rightarrow \mathbb{R}^n.$$

To make the problem-set closed, there should be n boundary conditions such that $R \in \mathbb{R}^n$. Considering small perturbations in the initial condition $\delta\bar{u}_0$ and parameter $\delta\bar{\lambda}_0$, and expanding in a Taylor series, we obtain the following, keeping only terms to first order in $\delta\bar{u}_0$ and $\delta\bar{\lambda}_0$,

$$\begin{aligned} R(\bar{u}_0, \bar{u}_1, \bar{\lambda}_0) + \frac{\partial R(\bar{u}_0, \bar{u}_1, \bar{\lambda}_0)}{\partial u_0} \delta\bar{u}_0 + \frac{\partial R(\bar{u}_0, \bar{u}_1, \bar{\lambda}_0)}{\partial u_1} \Phi(t_1, t_0; \bar{\lambda}) \delta\bar{u}_0 \\ + \frac{\partial R(\bar{u}_0, \bar{u}_1, \bar{\lambda}_0)}{\partial \lambda_0} \delta\bar{\lambda}_0 + \frac{\partial R(\bar{u}_0, \bar{u}_1, \bar{\lambda}_0)}{\partial u_1} \Phi_\lambda(t_1, t_0; \bar{\lambda}) \delta\bar{\lambda}_0 = 0. \end{aligned} \quad (13)$$

Here $R(\bar{u}_0, \bar{u}_1, \bar{\lambda}_0)$ is the residual vector, or out-of-balance vector [22]. It will gradually approach zero during the process to convergence. For convenience, we introduce the following two notations,

$$\begin{aligned} K_T &= \frac{\partial R(\bar{u}_0, \bar{u}_1, \bar{\lambda}_0)}{\partial u_0} + \frac{\partial R(\bar{u}_0, \bar{u}_1, \bar{\lambda}_0)}{\partial u_1} \Phi(t_1, t_0; \bar{\lambda}), \\ F_T &= \frac{\partial R(\bar{u}_0, \bar{u}_1, \bar{\lambda}_0)}{\partial \lambda_0} + \frac{\partial R(\bar{u}_0, \bar{u}_1, \bar{\lambda}_0)}{\partial u_1} \Phi_\lambda(t_1, t_0; \bar{\lambda}), \end{aligned} \quad (14)$$

where K_T is the known tangent stiffness matrix. Thus, the iteration process requires incremental solutions at the i th iteration step of the form,

$$\begin{aligned} (\delta\bar{u}_0)_i &= -K_T^{-1} (R - F\delta\bar{\lambda}_0) \\ &= \delta u_{Ri} + \delta u_{F}\delta\bar{\lambda}_i, \end{aligned} \quad (15)$$

where,

$$\delta u_R = -K_T^{-1} R, \quad \delta u_F = K_T^{-1} F_T. \quad (16)$$

In this case, at the i th iteration step, the displacement and load parameter are updated by

$$\begin{aligned} (\bar{u}_0)_k &= (\bar{u}_0)_{k-1} + (\Delta\bar{u}_0)_i, \\ (\bar{\lambda}_0)_k &= (\bar{\lambda}_0)_{k-1} + (\Delta\bar{\lambda}_0)_i. \end{aligned} \quad (17)$$

where the subscript k means the k th load step in the continuation process and it has the same meaning in the following text. Note that $(\Delta\bar{u}_0)_i$ is,

$$\begin{aligned} (\Delta\bar{u}_0)_i &= (\Delta\bar{u}_0)_{i-1} + (\delta\bar{u}_0)_i, \\ (\Delta\bar{\lambda}_0)_i &= (\Delta\bar{\lambda}_0)_{i-1} + (\delta\bar{\lambda}_0)_i, \end{aligned} \quad (18)$$

which we refer to as the *cumulative incremental displacement* and *cumulative incremental load*, respectively. Since the load parameter λ varies during the iteration, we need to

add an extra constraint to determine how the parameter changes. Riks [20] developed a pseudo arc-length method which searches the solution along the normal to the tangent with specific length to the converged equilibrium state. Crisfield [19] suggested a modified arc-length method which searches the solution along a hyper circular or spherical path. In this study, we follow the idea in [19]. Denoting the arc-length by ΔS , we use the following equation as the extra constraint,

$$(\Delta \bar{u}_0)_i^T (\Delta \bar{u}_0)_i = \|(\Delta \bar{u}_0)_i\|^2 = \Delta S^2. \quad (19)$$

where $\|\cdot\|$ denotes the usual norm in \mathbb{R}^n . Substituting the cumulative incremental displacement in (18) to (19), one can obtain the following quadratic algebraic equation in terms of increment of the load parameter,

$$a (\delta \bar{\lambda}_i)^2 + 2b (\delta \bar{\lambda}_i) + c = 0, \quad (20)$$

where

$$\begin{aligned} a &= \delta u_F^T \delta u_F, \\ b &= [(\Delta \bar{u}_0)_{i-1} + (\delta u_R)_i]^T \delta u_F, \\ c &= [(\Delta \bar{u}_0)_{i-1} + (\delta u_R)_i]^T [(\Delta \bar{u}_0)_{i-1} + (\delta u_F)_i] - (\Delta S)^2. \end{aligned}$$

For $b^2 - ac > 0$ in (20), there are two solutions which are given by

$$(\delta \bar{\lambda}_i)_{1,2} = \frac{-b \pm \sqrt{b^2 - ac}}{a}. \quad (21)$$

The two solutions of $\delta \bar{\lambda}_i$ determine two results of $(\Delta \bar{u})$, i.e. $(\Delta \bar{u})_{i1}$ and $(\Delta \bar{u})_{i2}$, which in turn lead to two directions on the equilibrium path, one going to a new path and the other one returning to the old path. To avoid ‘doubling back’ onto the old equilibrium path, the cumulative incremental displacement in the current and previous iteration steps, $(\Delta \bar{u})_i$ and $(\Delta \bar{u})_{i-1}$, should be positive which means [23],

$$\cos \theta = \frac{(\Delta \bar{u})_{i-1}^T (\Delta \bar{u})_i}{\|(\Delta \bar{u})_{i-1}\| \|(\Delta \bar{u})_i\|} = \frac{(\Delta \bar{u})_{i-1}^T (\delta \bar{u}_R)_i}{\|(\Delta \bar{u})_{i-1}\| \|(\delta \bar{u}_R)_i\|} > 0. \quad (22)$$

If both roots are positive, we choose the one that is closest to the linear solution,

$$\delta \bar{\lambda}_L = -\frac{c}{2b}. \quad (23)$$

In general, different sizes of arc-length ΔS will result in different numbers of iteration steps. To make the number of iterations constant, the arc-length can be adjusted by the following strategy,

$$\Delta S_k = \Delta S_{k-1} \frac{I_d}{I_{k-1}}, \quad (24)$$

where I_d is the desired number of iterations, usually smaller than 5. Based on our experience, I_d does not have to be an integer and can be varied to make the equilibrium path smoother. The first arc-length in the first load is computed by,

$$\Delta S_0 = \delta \lambda \sqrt{(\delta u_F)_1^T (\delta u_F)_1}. \quad (25)$$

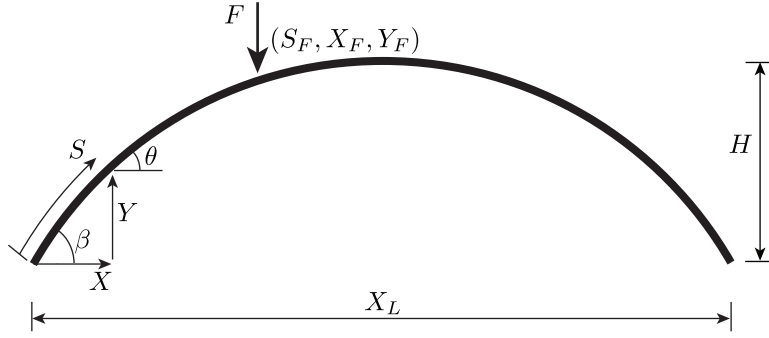


Figure 3: The schematic of a circular arch with length L , cross-sectional area A , span X_L and height H . Its bending stiffness is denoted by EI . The arch is subjected to a vertical concentrated force F with the position denoted by (S_F, X_F, Y_F) .

For subsequent load steps, the initial incremental load parameters are given by [23],

$$\delta\bar{\lambda}_0 = \frac{\Delta S_k}{\sqrt{\delta u_F^T \delta u_F}} \text{sgn} [(\Delta \bar{u})_{k-1}^T \delta \bar{u}_F]. \quad (26)$$

where $\text{sgn}[\cdot]$ is the sign function. After the cumulative incremental displacement converges to a stable value or the residual converges to a small prescribed tolerance, the iteration process stops for that load, and proceeds to the next load step.

3. Numerical results

After we clarified the principles of differential correction and arc-length continuation, we apply the algorithm to the structural mechanics, using the snap-through of arches and shallow spherical shells as examples. In order to compare the accuracy and convergence rate of the current algorithm, the continuation software package COCO will be used.

3.1. Snap-through of circular arches

As the first example, we study the snap-through of a circular arch with length L , span X_L , height H , cross-sectional area A and bending stiffness EI , as shown in Figure 3. From the left end of the arch, we use S , $X(S)$, $Y(S)$ to denote the arc length, horizontal and vertical coordinates. The angle in radians, measured counterclockwise from the horizontal, is denoted by $\theta(S)$. The internal forces along horizontal and vertical directions are denoted by $P(S)$, $Q(S)$, respectively, and the bending moment denoted by $M(S)$. The arch is subjected to a vertical concentrated force F with initial position (S_F, X_F, Y_F) . In this study, we assume the arch is slender so that the planar Euler *elastica*, which deals with uniform, thin, flexible and unsharable rod, is applicable to establish the governing differential equations. Based on the geometry, constitutive relation and equilibrium, the

differential equations are given by [24, 25],

$$\begin{aligned}
X_{,S} &= \cos \theta, \\
Y_{,S} &= \sin \theta, \\
EI (\theta_{,S} - \theta_{0,S}) &= M, \\
M_{,S} &= Q \cos \theta - P \sin \theta, \\
P_{,S} &= 0, \\
Q_{,S} &= 0,
\end{aligned} \tag{27}$$

where $\theta_0(S)$ is the initial shape of the arch. The comma in the subscript denotes the derivative with respect to the following coordinate. To make it more general, the following non-dimensional parameters are introduced

$$(s, x, y, s_F, x_F, y_F, x_L) = \frac{1}{L} (S, X, Y, S_F, X_F, Y_F, X_L), \quad m = \frac{ML}{EI}, \quad (p, q, f) = \frac{L^2}{EI} (P, Q, F), \tag{28}$$

where the arc-length of the arch is normalized to unity, i.e., $s \in [0, 1]$. The resulting non-dimensional differential equations are given by

$$\begin{aligned}
x_{,s} &= \cos \theta, \\
y_{,s} &= \sin \theta, \\
\theta_{,s} &= m + \theta_{0,s}, \\
m_{,s} &= q \cos \theta - p \sin \theta. \\
p_{,s} &= 0, \\
q_{,s} &= 0.
\end{aligned} \tag{29}$$

In this study, we consider a circular arch whose initial shape in the non-dimensional form is given by

$$\theta_0(s) = (1 - 2s)\beta, \quad \theta'_0(s) = -2\beta, \tag{30}$$

where β is the angle of the left end. In this study, two types of boundary conditions with in-plane immovable ends, i.e, pinned end and clamped end, are considered. The in-plane immovable boundary conditions are given by,

$$x(0) = y(0) = y(1) = 0, \quad x(1) = x_L. \tag{31}$$

Additional boundary conditions for the pinned or clamped ends are needed,

$$\begin{aligned}
m &= 0, \quad \text{for pinned ends,} \\
\theta &= \pm\beta, \quad \text{for clamped ends.}
\end{aligned} \tag{32}$$

The sign of θ depends on which end of the arch is clamped. If the left end is clamped, $\theta = +\beta$, otherwise we have $\theta = -\beta$.

For the concentrated force considered here, we decompose the arch into two parts at where the force is applied. Each sub-arch is governed by its differential equations and connected with the other by continuity conditions. Before we give the continuity relations, we rescale the domain of each sub-arch by its respective arc-length, s_F and

$1 - s_F$, respectively, so that each arch has unit arc-length measuring from the left end of each arch. In this study, we apply the concentrated force at a fixed point on the arch. Thus, the horizontal coordinate might change during the deformation. The continuity conditions of the two sub-arches are written by,

$$\begin{aligned} x_1(1) &= x_2(0), & y_1(1) &= y_2(0), & \theta_1(1) &= \theta_2(0), \\ m_1(1) &= m_2(0), & p_1(1) &= p_2(0), & q_1(1) - f &= q_2(0). \end{aligned} \tag{33}$$

where the subscript ‘1’ and ‘2’ denote the left and right sub-archs, respectively. Now the 12 first-order differential equations, along with 6 boundary conditions and 6 continuity conditions together are closed to be solved. It should be noted that in the non-dimensional governing differential equations of a circular arch based on *elastica* theory, the only appearing parameters are the end angle β and the boundary conditions. Other geometric and material parameters, such as the width and thickness of the cross-section, the Young’s modulus, do not appear. Another factor that affects the deformation is the location of the vertical concentrated force.

In fact, the force can also be applied at a fixed horizontal coordinate. In this case, the arc-length of each sub-arch might change in the loading history. Before the implementation of differential correction, we need to rescale the domain of sub-arches to unity so that the true arc-length of each arch will explicitly appear in the governing equations behaving as a parameter. Here we also consider the arc-length of each arch as a state variable whose derivative with respect to s is zero. In this case, we have an extra differential equation written by, $s_{F,s} = 0$. On this condition, the continuity condition $x_1(1) = x_2(0)$ should be corrected to be $x_1(1) = x_2(0) = x_F$. Again, x_F is the fixed horizontal coordinate of the location of the applied vertical force. A similar situation exists when differential correction is applied to compute the periodic orbits in an autonomous system [4, 11, 12]. In such problems, the period is unknown beforehand which will be corrected during iteration. We can consider the period as a parameter or a state variable [26, 27].

Comparison.. We start the numerical results by giving a comparison with published results [28–30] of a pinned-clamped deep circular arch subjected to a vertical concentrated force at the crown. The central angle of the arch is 215° . In this case, $\beta = 107.5^\circ$ which is the only parameter we need to assign to the non-dimensional governing equations. This example was first studied in [31] and then attracted tremendous study using different beam or arch models. Abundant data can be obtained so that it is easy to compare the results obtained by differential correction with references among which we select Refs. [28–30]. Figure 4 gives the load-displacement relations, where both horizontal and vertical displacements are included. From the comparison, excellent agreement between current results and references is observed, which demonstrates our manipulation is reasonable and numerical computation is accurate. More good comparisons can be found in [32–37] which are not given here for simplicity. It should be mentioned that along the equilibrium path, self-contact was observed which cannot physically occur in practical experiments, as also reported in [28]. For comparison, we ignore this impossibility and give the whole equilibrium path.

Numerical results of semicircular arches.. In this part, we give the numerical results of snap-through buckling of semicircular arches [38, 39] as shown in Figure 5. The vertical

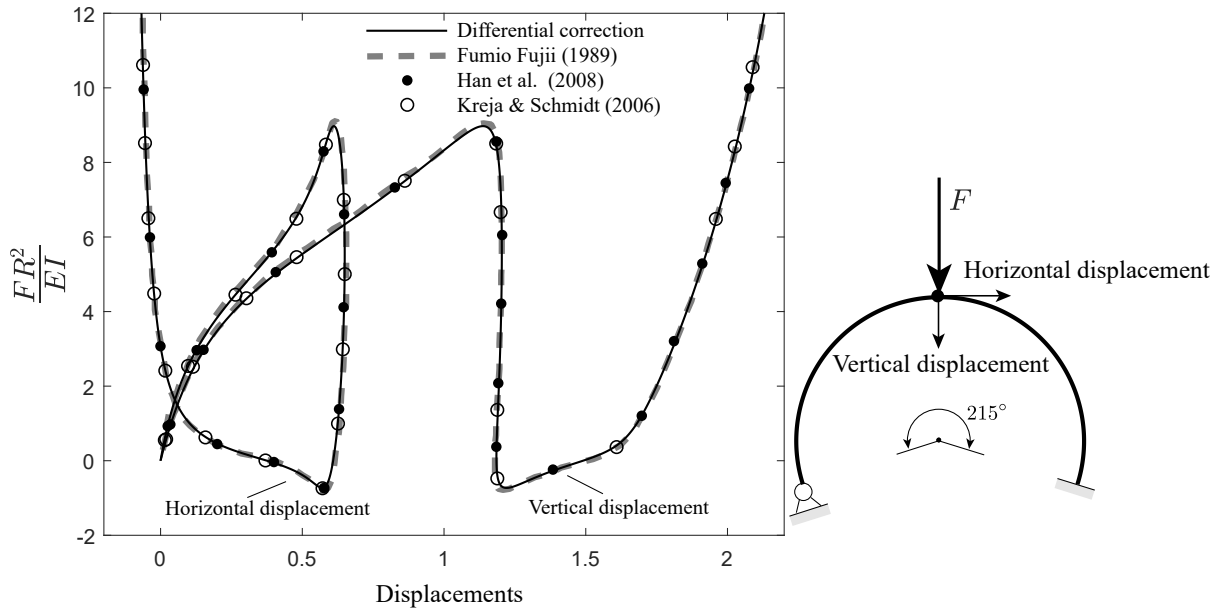


Figure 4: Comparison of the load-displacement relation of a pinned-clamped circular arch obtained by differential correction with references [28–30]. The arch with central angle equal to 215° is subjected to a vertical concentrated load at the apex. Here R is the radius of the circular arch. Notice that in this figure the load is rescaled, while the displacements keep consistent as before.

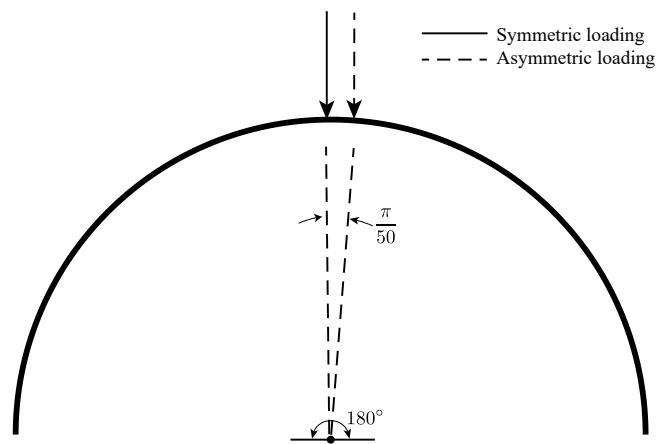


Figure 5: Schematic of a semicircular arch subjected to a vertical concentrated force. In the corresponding numerical examples, the force will be applied at two locations: the first one is a symmetric case where the force is applied at the crown of the arch; the second one is an asymmetric case where the force is applied with an offset angle ($\pi/50$) from crown. Moreover, different boundary conditions will be considered, including pinned and clamped ends.

concentrated force will be applied in two cases: the symmetric and asymmetric forces. The symmetric force is applied at the crown of the arch, while the asymmetric force is

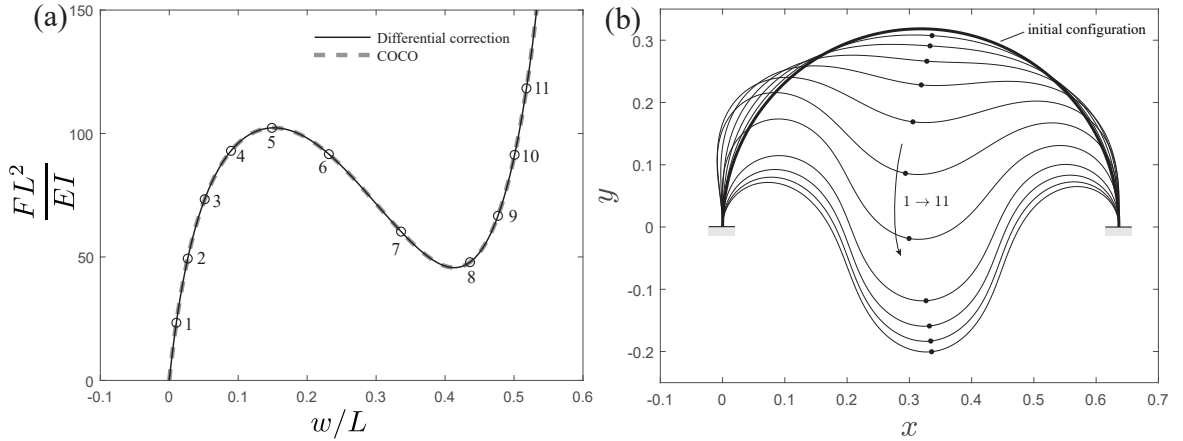


Figure 6: Example of a clamped-clamped semicircular arch subjected to an asymmetric force. In (a) it gives the load-displacement relation. The results obtained by differential correction agree well with those obtained by COCO. Along the equilibrium path, we select 11 points, denoted by circles, to show the corresponding configurations. In (b) the configuration of each point selected along the equilibrium path is shown, where the black dots denote the location of the force during the deformation process.

applied at slightly offset location to the crown with offset angle valued at $\pi/50$. For comparison, the results obtained by COCO will also be given.

Figure 6 gives the force-displacement relation and some configurations on the equilibrium path of a clamped-clamped arch subjected to an asymmetric force. Here and in the following, the displacements in the load-deflection relation are measured at the point where the force is applied. The horizontal and vertical displacements at that point are denoted by u and w , respectively. Figure 6(a) is a typical snap-through scenario in curved structures. In the force-displacement relation, initially the vertical displacement increases with the increment of the applied force until it reaches the local maximum. Then the displacement keeps increasing, while the load decreases until it reaches the local minimum. Finally, the displacement increases again with the continued application of force. On this equilibrium path, the local maximum and minimum are usually called limit points. If the force is applied via a displacement-controlled device, the full equilibrium path can be detected [40, 41]. However, if the force is applied via a load-controlled device, the situation is different. The force can be increased until it reaches the upper limit point. Once the load is further increased, no matter how small it is, the arch will directly snap-through with a sudden and fast dynamic jump to its inverted configuration, since there is no longer any locally available stable equilibrium state. In Figure 6(a), 11 points marked as circles are selected on the equilibrium path. Each point represents a possible equilibrium path. The corresponding configuration is shown in Figure 6(b) from which we can notice the deformation is asymmetric.

Figure 7(a) shows the force-displacement relation of a pinned-clamped semicircular arch. It can be seen from the figure that this equilibrium path is more complicated than that in Figure 6(a). Here, the snap-back behavior occurs and, moreover, the looping type equilibrium path appears. Two more limit points exist, compared with the previous case,

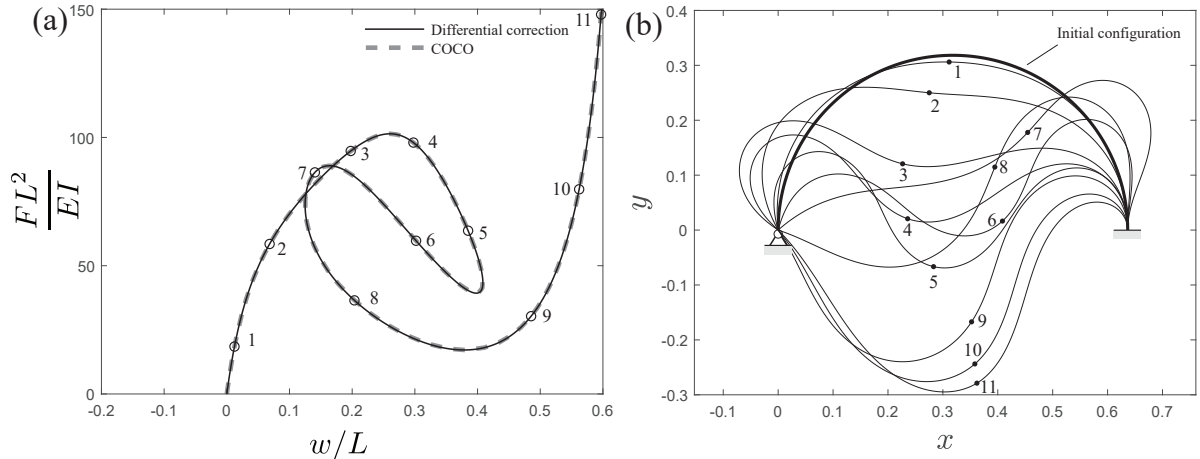


Figure 7: Example of a semicircular arch with pinned-clamped boundary subjected to a symmetrical force. (a) and (b) are the force-displacement relation and configurations of equilibrium states on the equilibrium path, respectively. [42] also predicted close results for force-displacement relation, but in different scaling.

which separate the equilibrium into five branches among which two remote equilibrium states are stable, and the other three in the middle are unstable. Close results were predicted by [42], but were given in a different scaling. To show the configurations on the equilibrium path, 11 points denoted by circles are selected on the force-displacement relation and the corresponding configurations are shown in Figure 7(b). From the configurations, we notice that once the load is applied, the apex begins to deflect and the left end of the arch rotates in a counterclockwise direction. However, the arch cannot directly snap-through to the inverted configuration just by continuing to rotate along the counterclockwise direction due to physical and geometrical constraints. After the force-displacement relation reaches the first snap-back point, the reconfiguration begins which makes the left end rotate in a clockwise direction and pushes the center to the upper right direction. When the equilibrium path arrives at the second turning point, the whole structure gradually moves downward to the inverted configuration. As anticipated, the asymmetric boundary conditions induce asymmetric deformation.

The examples given in Figures 6 and 7 show asymmetric deformation, induced by the asymmetric loading and boundary conditions, respectively. COCO does not find any bifurcation point (the intersection of two or more equilibrium paths) in these simulations, indicating both snap-throughs occur at a limit point. Similar conclusions were given in [43]. In the next example we will present the semicircular arch with symmetric boundary constraints subjected to symmetric force at the crown. As pointed out in [17], in the deflection of a deep arch, the pitchfork bifurcation may appear before the limit point. The asymmetric deformation [44] might exist which is another type of asymmetric deformation.

It should be noted that the current algorithm cannot predict the bifurcation point so that only the primary branch of the equilibrium paths can be followed. Thus, we first present the symmetric snap-through of a pinned-pinned semicircular arch subjected to a symmetric force at the crown, as shown in Figure 8. The force-displacement relation shows

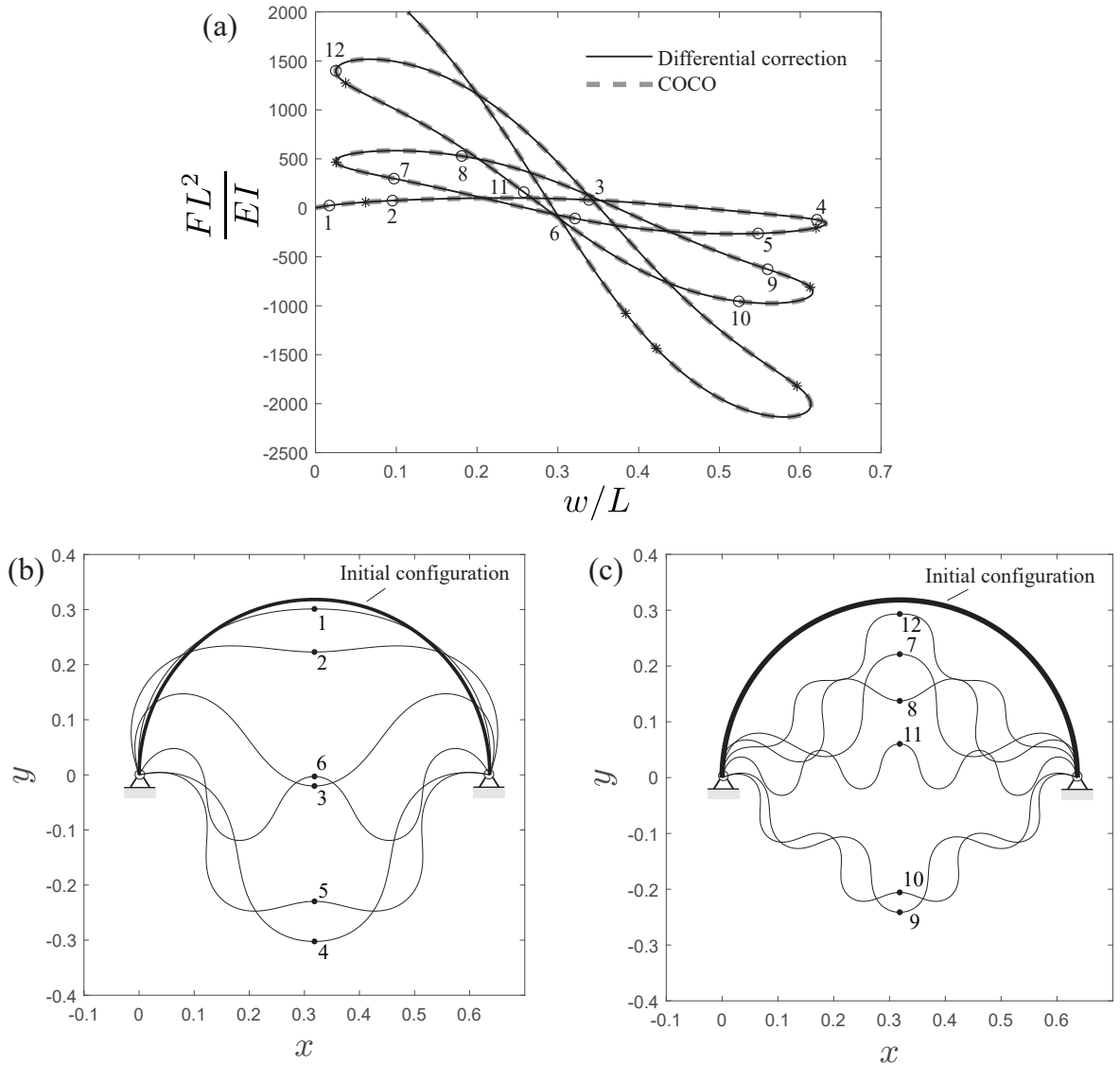


Figure 8: Example of the primary equilibrium path of a semicircular arch with pinned-pinned boundary subjected to symmetric concentrated force at the crown. (a) is the force-displacement relation. The curve presents a looping path with increment of flexuosity in configurations. (b) and (c) show the configurations on the equilibrium path where all configurations are symmetric.

a looping type of curve with multiple snap-back points which is much more complicated than Figure 7(a). From the configurations of 12 points selected on the equilibrium path, as shown in Figure 8(b) and Figure 8(c), symmetric deformation patterns are observed. The increment of the loop is accompanied with the increase of the wave number and the configurations become more flexuous, as also pointed out by [45, 46]. On the equilibrium path shown in the figure, COCO detects 8 bifurcation points, marked as stars, among which the first one appears before the first limit point. It implies asymmetric branch might occur at the bifurcation point. Other bifurcation points are the bifurcations at higher order modes. Ref. [45] predicts close results. Readers are referred to the paper for details.

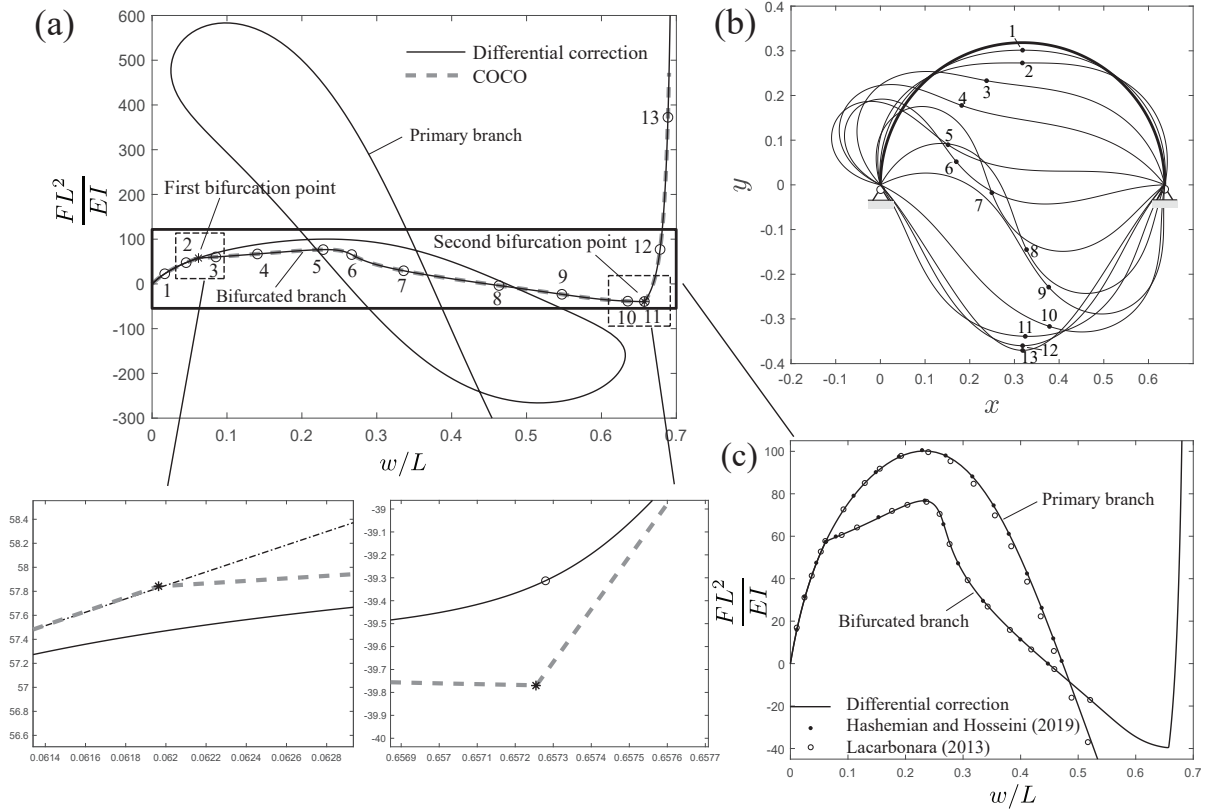


Figure 9: Example of the bifurcated equilibrium path of a semicircular arch with pinned-pinned ends subjected to concentrated force at the crown. (a) gives the primary and bifurcated equilibrium paths. The two stars on the secondary equilibrium path are the two bifurcation points, giving the bifurcated path into three parts where the left and right parts are symmetrical deformation, while the middle part is asymmetrical deformation. The two panels at the bottom show the zoom-in view around the bifurcation points. (b) shows the configurations of the equilibrium states on the secondary equilibrium path. (c) gives the comparisons with [47, 48] which shows a good agreement.

Although the current algorithm cannot predict the bifurcations, it is possible to trace the asymmetric deformation. A commonly adopted way is to break the symmetry in the system (as already indicated in the previous two examples): either the symmetries of initial configuration or those of the applied load. In the buckling of flat plates, small imperfections [49] can be added so that the geometric symmetry can be broken, while in the snap-through of curved structures, small horizontal loads can be added so that the symmetry in the load can be destroyed [47, 50]. For proper imperfections, the bifurcated equilibrium path can be well approximated. However, extremely large values might produce a significant difference from the true equilibrium path of asymmetric deformation, while extremely small values can prevent the equilibrium path from switching to the asymmetric deformation. Moreover, based on our experience, the desired iteration step I_d will also affect the selection of initial imperfection. Here in the current problem, we add a very small horizontal load at the crown of the arch, i.e., $0.07\%f$. Figure 9 gives the bifurcated branch of a pinned-pinned semicircular arch subjected to symmetric loading. From the force-displacement relation in Figure 9(a), at the beginning of the

loading process, the displacement increases with the increment of the external force and the deformation is symmetric. When it reaches the area around the first bifurcation point, the asymmetric deformation gradually becomes obvious. Before the first limit point, the equilibrium state is still stable. The displacement and force both increase. After the first limit point, the force decreases while the displacement keeps increasing. This process is unstable. Finally after the second bifurcation point, the arch deflects to its inverted symmetric configuration. The two panels at the bottom of Figure 9(a) give the close-up around the bifurcation points. From the configurations in 9(b), we find the configurations of points 1, 2, 12, and 13 are symmetric, while other configurations are asymmetric. We also notice COCO exactly predicts the bifurcation points which are cusps connecting the symmetric and asymmetric branches of the equilibrium path. However, since the small horizontal external force is applied at the crown in differential correction, the bifurcation point disappears making the equilibrium path smooth. Nevertheless, the results obtained by differential correction and COCO match well with each other. Figure 9(c) gives an additional comparison with [47, 48]. Good agreement is observed which demonstrates the validation of the current results.

After we investigate the symmetric case of the pinned-pinned semicircular arch, we analyze the asymmetric case. Figure 10 gives the asymmetric deformation of a pinned-pinned semicircular arch subjected to an asymmetric force. The equilibrium path shows a looping curve. Due to the asymmetric loading position, the configuration during the deformation process is asymmetric. The wave number increases with the increment of the load, as shown in Figures 10(b) and 10(c). In the current asymmetric case, the offset angle is merely $\pi/50 \approx 0.0628$, but it makes the equilibrium path quite different from the symmetric case shown in Figure 8. Combining with the example to obtain the secondary equilibrium path in Figure 9, we find that the process of computing the equilibrium path for the deep circular arch is very sensitive to perturbations, such as the offset distance from the apex and the disturbance in the horizontal force. The small disturbance can transfer the equilibrium path to different branches. Ref. [45] presents close results with a good agreement with the current algorithm; readers are referred to it for the details.

3.2. Snap-through of shallow spherical caps

In this section, we present another example of the axisymmetric deformation of a shallow spherical shell. The thickness, radius, span, and height of the spherical shell are denoted by h , R , L and H , respectively. Due to the special geometry of the spherical shell, the polar coordinate system is used to describe the deformation in which r and θ are the axial and circumferential directions, and z is the vertical direction pointing downward. In the axisymmetric case, the in-plane shear stresses and the displacement along the circumferential direction vanish and we only need to consider the displacements along axial and vertical directions, denoted by $u(r)$ and $w(r)$, respectively. In the polar coordinate system, the governing equations for shallow shells [51] are given by,

$$(rN_r)_{,r} - N_\theta = 0, \quad (34a)$$

$$(rQ_r)_{,r} + (rw_{,r}N_r)_{,r} + \frac{r}{R}(N_r + N_\theta) + qr = 0, \quad (34b)$$

$$(rM_r)_{,r} - M_\theta - rQ_r = 0, \quad (34c)$$

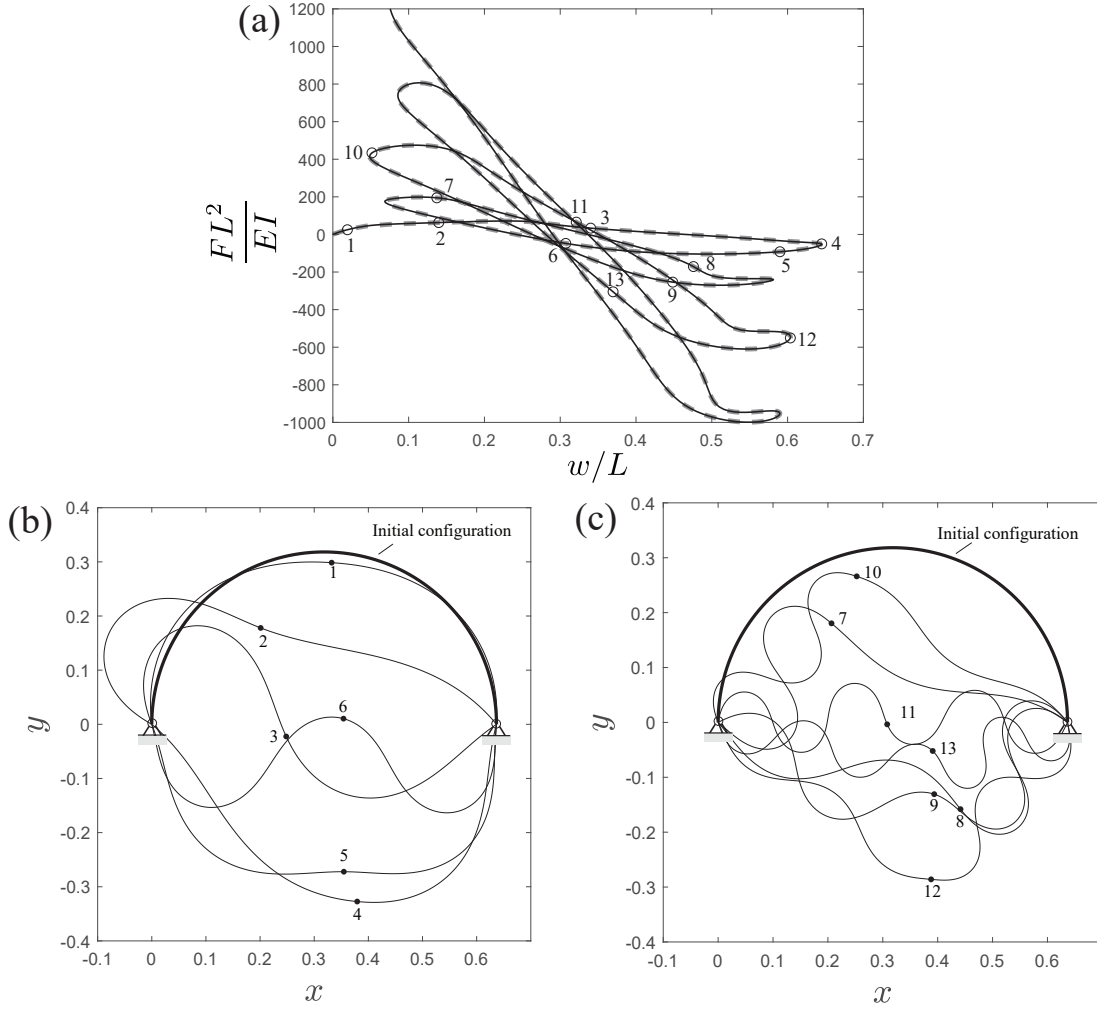


Figure 10: Example of a semicircular arch with pinned-pinned boundary subjected to an asymmetrical force. (a) gives the force-displacement relation, which presents a looping type of curve with multiple snap-back points. In the results, no bifurcations are detected by COCO. (b) and (c) show the configurations of different equilibrium states on the equilibrium path. In the current case study, asymmetric deformation is observed. With the increment of the loops, the wave number of the configuration increases.

where N_r and N_θ are the radial and circumferential stress resultants; M_r and M_θ are the radial and circumferential bending moment resultants; Q_r is the transverse shear force; q is the applied transverse force. From the constitutive equations, the forces and moments are given by

$$\begin{pmatrix} N_r \\ N_\theta \end{pmatrix} = A \begin{pmatrix} 1 & \nu \\ \nu & 1 \end{pmatrix} \begin{pmatrix} \epsilon_r^0 \\ \epsilon_\theta^0 \end{pmatrix}, \quad \begin{pmatrix} M_r \\ M_\theta \end{pmatrix} = -D \begin{pmatrix} 1 & \nu \\ \nu & 1 \end{pmatrix} \begin{pmatrix} \kappa_r \\ \kappa_\theta \end{pmatrix}, \quad (35)$$

where $A = Eh/(1 - \nu^2)$ and $D = Eh^3/[12(1 - \nu^2)]$ are the tensile and bending stiffnesses; ν denotes the Poisson's ratio; ϵ^0 and κ are the strains and curvatures on the mid-plane

given by,

$$\begin{aligned} \epsilon_r^0 &= u_{,r} - \frac{w}{R} + \frac{1}{2}w_{,r}^2, & \epsilon_\theta^0 &= \frac{u}{r} - \frac{w}{R}, \\ \kappa_r &= w_{,rr}, & \kappa_\theta &= \frac{w_{,r}}{r}. \end{aligned} \quad (36)$$

By using (34a), we rewrite (34b) as

$$(rQ_r)_{,r} + (rw_{,r}N_r)_{,r} + \frac{(r^2N_r)_{,r}}{R} + qr = 0. \quad (37)$$

Integrating (37) yields

$$rQ_r + rw_{,r}N_r + \frac{r^2N_r}{R} + \int_0^r qxdx = 0. \quad (38)$$

Substituting (34c) into (34b), and applying the constitutive relations in (35) and the nonlinear strain-displacement relations in (36) to (34a) and (34b), we obtain the equilibrium equations in terms of the displacements as

$$\begin{aligned} u_{,rr} + \frac{u_{,r}}{r} - \frac{u}{r^2} - \frac{1+\nu}{R}w_{,r} + \frac{1-\nu}{2r}w_{,r}^2 + w_{,r}w_{,rr} &= 0, \\ w_{,rrr} + \frac{w_{,rr}}{r} - \frac{w_{,r}}{r^2} - \frac{1}{Dr} \int_0^r qrdx - \frac{12w_{,r}}{h^2} \left(u_{,r} - \frac{w}{R} + \frac{1}{2}w_{,r}^2 + \frac{\nu u}{r} - \frac{\nu w}{R} \right) \\ - \frac{12r}{Rh^2} \left(u_{,r} - \frac{w}{R} + \frac{1}{2}w_{,r}^2 + \frac{\nu u}{r} - \frac{\nu w}{R} \right) &= 0. \end{aligned} \quad (39)$$

When the radius of the spherical caps grows to infinity, we can degenerate (39) to obtain the equations of motion for circular plates [52]. For different types of constraints at the edge, the boundary conditions are written by

$$\begin{cases} N_r(L) = w(L) = M_r(L) = 0, & \text{for a movable simply-supported edge,} \\ u(L) = w(L) = M_r(L) = 0, & \text{for an immovable simply-supported edge,} \\ N_r(L) = w(L) = w_{,r}(L) = 0, & \text{for a movable clamped edge,} \\ u(L) = w(L) = w_{,r}(L) = 0, & \text{for an immovable clamped edge.} \end{cases} \quad (40)$$

We still need two boundary conditions, the symmetric conditions at the apex or the origin, which are

$$u(0) = w_{,r}(0) = 0. \quad (41)$$

In this case, the system consists of one second-order and one third-order differential equations associated with five boundary conditions which are complete and ready to be solved. We introduce the following non-dimensional parameters,

$$\bar{r} = \frac{r}{L}, \bar{w} = \frac{w}{h}, \bar{u} = \frac{uL}{h^2}, \alpha = \frac{L^2}{Rh}, \gamma = 6(1-\nu^2), \bar{q} = \frac{qL^4}{Eh^4}. \quad (42)$$

and consider uniformly distributed pressure so that the governing equations are written in non-dimensional form as

$$\begin{aligned} u_{,rr} + \frac{u_{,r}}{r} - \frac{u}{r^2} - (1+\nu)\alpha w_{,r} + \frac{1-\nu}{2r}w_{,r}^2 + w_{,r}w_{,rr} &= 0, \\ w_{,rrr} + \frac{w_{,rr}}{r} - \frac{w_{,r}}{r^2} - 12(w_{,r} + \alpha r) \left(u_{,r} - \alpha w + \frac{1}{2}w_{,r}^2 + \frac{\nu u}{r} - \nu\alpha w \right) - \gamma q &= 0. \end{aligned} \quad (43)$$

where the bars over certain variables are ignored for convenience. The boundary conditions in (40) now are measured at $r = 1$. In order to apply differential correction, we introduce the following notations

$$u_0 = u, \quad u_1 = \dot{u}_0, \quad w_0 = w, \quad w_1 = \dot{w}_0, \quad w_2 = \dot{w}_1,$$

which puts the equations in (43) into a first order form, with column vector $z = (u_0, u_1, w_0, w_1, w_2)^T$, written by

$$\dot{z} = f, \tag{44}$$

where f is,

$$f = \begin{pmatrix} u_1 \\ -\frac{u_1}{r} + \frac{u_0}{r^2} + (1 + \nu)\alpha w_1 - \frac{1-\nu}{2r}w_1^2 - w_1w_2 \\ w_1 \\ w_2 \\ -\frac{w_2}{r} + \frac{w_1}{r^2} + 12(w_1 + \alpha r)\left(u_1 - \alpha w_0 + \frac{1}{2}w_1^2 + \frac{\nu u_0}{r} - \nu\alpha w_0\right) + \gamma qr \end{pmatrix}. \tag{45}$$

When applying differential correction, we need to expand the boundary conditions at $r = 1$. Using the simply supported edge as an example, we have

$$\begin{aligned} u_0(1) + \Phi_{11}\delta u_0 + \Phi_{12}\delta u_1 + \Phi_{13}\delta w_0 + \Phi_{14}\delta w_1 + \Phi_{15}\delta w_2 + \Phi_{\lambda_1}\delta\lambda &= 0, \\ w_0(1) + \Phi_{31}\delta u_0 + \Phi_{32}\delta u_1 + \Phi_{33}\delta w_0 + \Phi_{34}\delta w_1 + \Phi_{35}\delta w_2 + \Phi_{\lambda_3}\delta\lambda &= 0, \\ w_2(1) + \Phi_{51}\delta u_0 + \Phi_{52}\delta u_1 + \Phi_{53}\delta w_0 + \Phi_{54}\delta w_1 + \Phi_{55}\delta w_2 + \Phi_{\lambda_5}\delta\lambda &= 0. \end{aligned} \tag{46}$$

Since $u_0(0) = w_1(0) = 0$ can be exactly satisfied, we set $\delta u_0 = \delta w_1 = 0$. In this case, we have

$$R = \begin{pmatrix} u_0(1) \\ w_0(1) \\ w_2(1) \end{pmatrix}, \quad F = \begin{pmatrix} \Phi_{\lambda_1} \\ \Phi_{\lambda_3} \\ \Phi_{\lambda_5} \end{pmatrix}, \quad K_T = \begin{pmatrix} \Phi_{12} & \Phi_{13} & \Phi_{15} \\ \Phi_{32} & \Phi_{33} & \Phi_{35} \\ \Phi_{52} & \Phi_{53} & \Phi_{55} \end{pmatrix}, \tag{47}$$

which are the residual vector, tangent force vector, and tangent stiffness matrix, respectively, which can be obtained by simultaneous numerical integration. The state transition matrix for the current problem can be obtained from the variational equations

$$\dot{\Phi} = Df(z)\Phi \quad \text{with } \Phi(0; z_0, q) = I_5, \tag{48}$$

where $z_0 = z(0)$ are the boundary conditions at the origin which is used as the initial conditions in the differential correction process. $Df(z)$ is the Jacobian matrix of the flow field f in (45) evaluated along the reference trajectory written by,

$$Df(z) = \begin{pmatrix} 0 & 1 & 0 & 0 & 0 \\ \frac{1}{r^2} & -\frac{1}{r} & 0 & Df_{24} & -w_1 \\ 0 & 0 & 0 & 1 & 0 \\ 0 & 0 & 0 & 0 & 1 \\ \frac{12\nu(w_1 + \alpha r)}{r} & 12(w_1 + \alpha r) & Df_{53} & Df_{54} & -\frac{1}{r} \end{pmatrix}. \tag{49}$$

where

$$\begin{aligned} Df_{24} &= (1 + \nu)\alpha - \frac{1-\nu}{r}w_1 - w_2, & Df_{53} &= -12\alpha(w_1 + \alpha r)(1 + \nu), \\ Df_{54} &= \frac{1}{r^2} + 12\left(u_1 - \alpha w_0 + \frac{1}{2}w_1^2 + \frac{\nu u_0}{r} - \nu\alpha w_0\right) + 12w_1(w_1 + \alpha r). \end{aligned}$$

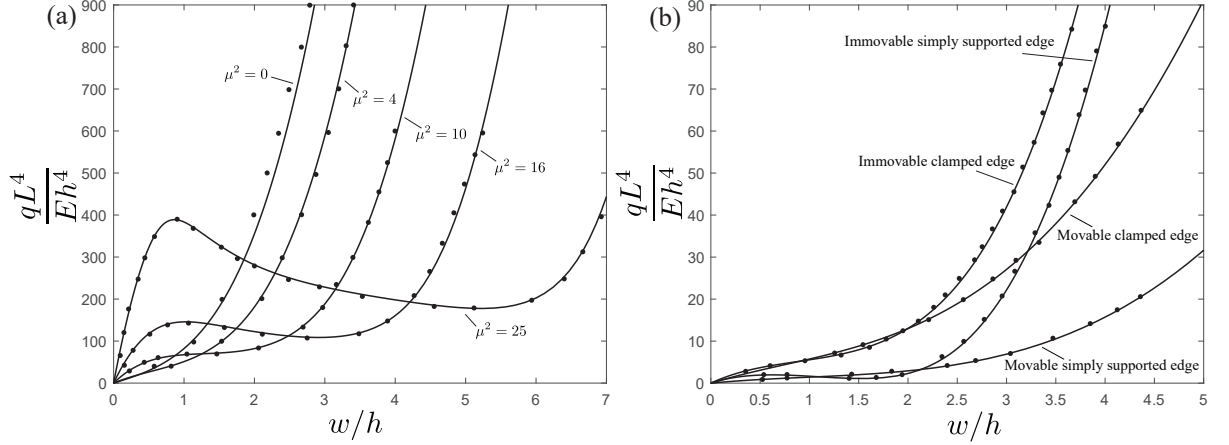


Figure 11: Comparison between the results obtained by differential correction and [53, 54]. (a) shows the comparison of an immovable clamped shallow spherical shell [53]. The geometrical parameter μ^2 is defined by $\mu^2 = \sqrt{12(1 - \nu^2)}L^2/(Rh)$ and the load is rescaled by $qL^4m^6/(4Eh^4)$, where $m^4 = 12(1 - \nu^2)$. The Poisson's ratio is taken as $\nu = 0.32$. Current results are consistent with [53]. Good results are also given in [55] which are not shown here for simplicity. (b) shows the comparison of shallow spherical shells with different boundary conditions ($\alpha = 1, \nu = 0.3$) [54].

On the other hand, Φ_λ can be obtained by solving the following equations,

$$\dot{\Phi}_\lambda = Df\Phi_\lambda + D_\lambda f, \quad \text{with } \Phi_\lambda(0; z_0, q) = 0, \quad (50)$$

where

$$D_\lambda f = (0, 0, 0, 0, \gamma r)^T. \quad (51)$$

Now we are ready to implement differential correction and the arc-length continuation to get the equilibrium path of the snap-through of the shallow spherical shell. Integrating (44), (48) and (50) along the length of the arch, we can obtain the $z(1)$, $\Phi(1)$ and $\Phi_\lambda(1)$ which will be assigned to (47). Note that when applying the integration, the origin is a singular point. To avoid the singularity there, we should integrate the equations from a small perturbation Δr to the origin, like 10^{-5} , so that the integration time will be $r \in (\Delta r, 1)$.

Comparisons.. The numerical results begin with giving comparisons with [53, 54]. Figure 11(a) gives the comparison of an immovable clamped shallow spherical shell of different geometrical sizes with [53]. The equilibrium equations in [53] are given by momenta equation and compatibility equation in terms of the deflection and stress function. For the case $\mu^2 = 0$, it is the nonlinear axisymmetric bending of a flat circular plate. Figure 11(b) shows the comparison of shallow shells with different boundary conditions with [54]. In this comparison the parameters are selected as $\alpha = 1$ and $\nu = 0.3$. From the comparisons, good consistency between current results and [53, 54] is observed, indicating the validity of the current model and algorithm.

Numerical results.. In the numerical results, we discuss the effects of boundary conditions and geometrical parameters on the snap-through of shallow spherical shells. Figure 12 shows the force-displacement relation of shells with different boundary conditions: (a)

immovable clamped edge, (b) movable clamped edge, (c) immovable simply-supported edge, (d) movable simply-supported edge. It can be seen from the figure that if the shell is too shallow, such as $\alpha = 1$, the shell behaves similarly to a flat plate, that the lateral deflection increases monotonously with the increment of the uniform pressure, whatever the boundary condition is. For such geometrical parameters, no snap-through occurs. When the height of the shell increases, the shell with an immovable simply-supported boundary is most likely to have snap-through buckling, while the shell with a movable clamped boundary is least likely. For α varying from 1 to 4, only the shell with an immovable simply-supported edge has bistable equilibria; they are indicated by the negative pressure in the force-displacement relation. Compared with other types of boundary conditions, the movable simply-supported shell is the easiest to deform. Even small pressure can induce much larger deflection than the shells with other boundary conditions, which means it has the lowest overall stiffness. Note that in the current case studying the shallow spherical shells, no snap-back behavior or looping type of force-displacement relation exists. Since we only consider the axisymmetric deformation of the shallow spherical shell, no bifurcation points are expected. Good agreement of results between the current algorithm and COCO is observed which shows the accuracy and robustness of the current approach.

3.3. Discussions

After presenting the snap-through behaviors of arches and shallow spherical shells, we have a clear picture about differential correction. In the process of the implementation of differential correction to solve boundary-value problems, we need to know the conditions at one boundary that we want to target, including the final state of the trajectory and the state transition matrix, which can be obtained by simultaneously integrating the governing equations and variational equations. By giving the initial guesses of the boundary conditions, we can begin the continuation process to update the boundary conditions at the other end used as the initial conditions in the differential correction process. Since the iteration process aims to search for the correct boundary conditions, the dimension of the matrix is at most equal to the number of the state variables (or the boundary conditions). Because some of the boundary conditions can be automatically satisfied, generally the dimension of the matrix is lower than the state variables.

However, in discretization methods, such as the finite element method, orthogonal collocation method, and mesh-free method, et al., the dimension of the matrix will be the number of the state variables multiplied by the number of nodes or sampling points in the domain. The huge storage of node information slows down the iteration process and increases the computational time. The more sampling points we mesh, the worse the situation will be. Due to the large dimension of the tangent stiffness matrix in such algorithms, the tangent stiffness matrix is only updated at a certain preselected steps of the iteration in order to cut down the computation cost. Although it needs more iteration steps for convergence, the computation time should be less. However, the dimension of the tangent stiffness matrix in differential correction is constant and is much lower than that of the discretization methods. It can be updated at every iteration step, making it fast to converge. The only factor that slows down the computation is the numerical integration of the equations of motion and variational equations. Another advantage of differential correction is its easy implementation. No matter what the problems are, we use the same

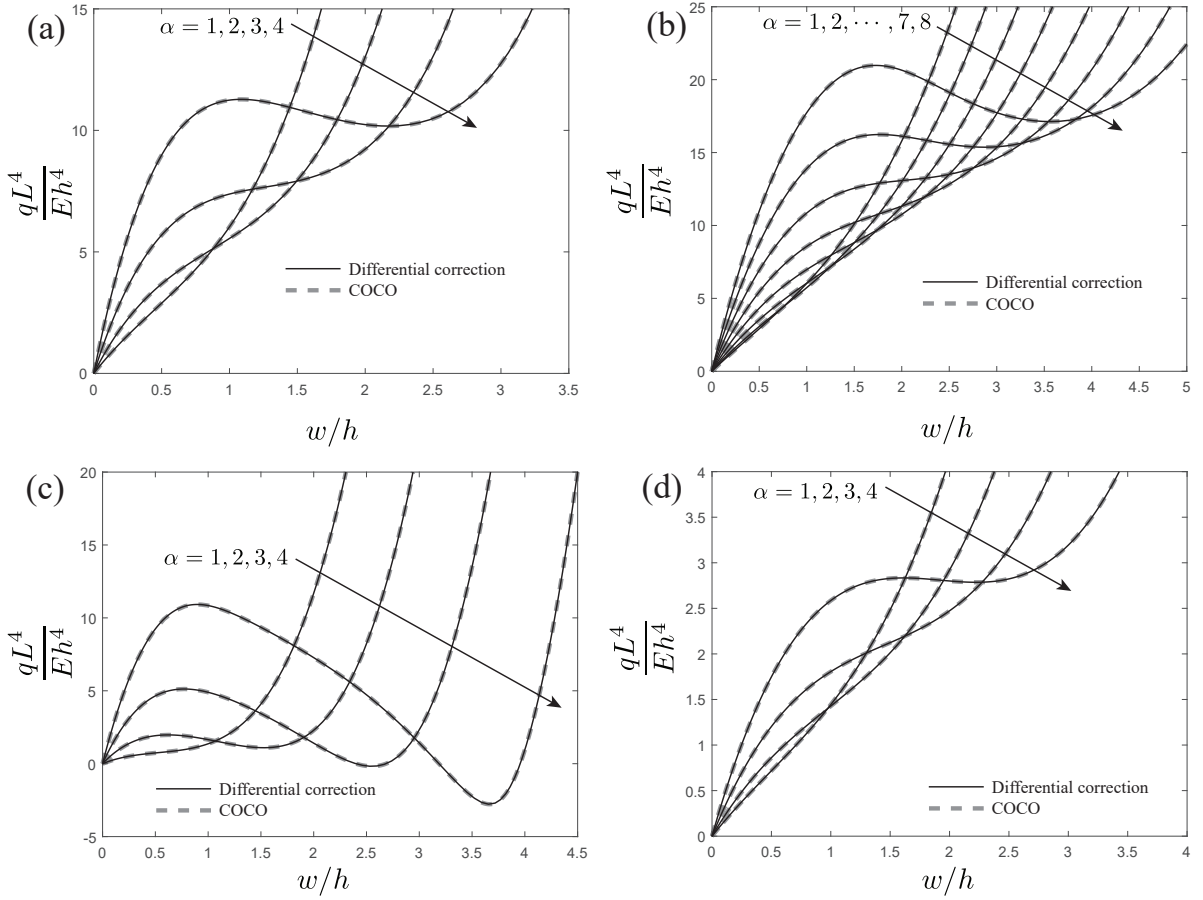


Figure 12: Force-displacement relation of shallow spherical caps with different boundary conditions and geometry: (a) an immovable clamped edge, (b) a movable clamped edge, (c) an immovable simply-supported edge, and (d) a movable simply-supported edge. In this figure, the Poisson's ratio is $\nu = 0.3$. The results obtained by differential correction and COCO agree well with each other. Close results for the four types of boundary conditions of shallow spherical shells with $\alpha = 2$ were also predicted by [54].

core of the arc-length continuation. Once it is established, it does not need to be updated. For different boundary value problems, we only need to work on the governing equations and variable equations to prepare the tangent stiffness matrix, tangent force vector and the residual vector which will be used in the arc-length continuation.

Based on our experience, the implementation of differential correction is as simple as COCO, and they predict consistent results. However, one unavoidable flaw of differential correction, compared with COCO, is its inability to detect bifurcations. Fortunately, a sophisticated strategy of breaking the symmetry in the initial configuration and load makes it possible to get the bifurcated branches of the equilibrium paths. Another shortcoming of differential correction, which cannot be avoided, is its inability to solve partial differential equations with respect to two dimensional spatial coordinates. As for the partial differential equations with respect to one dimensional spatial derivative and one dimensional time derivative, differential correction is applicable disposing of the time derivative by using the Newmark method.

4. Conclusions

In this paper, we extend the application of differential correction along with arc-length continuation to structural mechanics, the examples of the boundary-value problems. The detailed derivations of the present algorithm are given. Two examples about the snap-through of arches and shallow spherical shells are given to show the process of the implementation of differential correction and arc-length continuation. This method is capable of passing the limit points and turning points, enabling the computation of complicated equilibrium paths. Compared with other discretization schemes, the current algorithm involves a low dimensional matrix calculation, saving storage space and speeding up computation. In the meantime, the off-the-shelf continuation tool COCO was adopted to compare with our scheme. The results obtained by the present algorithm and COCO are consistent, showing the accuracy and robustness of the current algorithm.

From the numerical examples, we find that a small asymmetry in boundary conditions and loading, such as a slight offset of location or tiny off-axis-of-symmetry force component, can destroy the symmetrical deformation of the structures. This gives us a strategy, breaking the symmetry of the system by introducing the small imperfection of the configuration and load, to trace the existing bifurcated branches of the equilibrium path which commonly exist in symmetrical deep curved structures. On the other hand, snap-through does not exist in structures which are too shallow. Boundary conditions will significantly affect the snap-through behavior. Deep structures might have a looping type of equilibrium path with multiple turning points, while shallow structures present much a simpler equilibrium path.

In the current study, we just considered the axisymmetric shallow shell model so that only limited mechanical behavior can be predicted. However, the shell-type structures are sensitive to boundary conditions, geometrical parameters, and initial geometrical imperfection. Only a more general asymmetric model can detect more complicated deformation patterns. In future work, we will use a general shell model to study the deformation, which will reveal more interesting phenomena. Additionally, the ability to predict bifurcation in differential correction should also be considered.

Acknowledgments

This work was supported in part by the National Science Foundation under award 1537349. The authors would like to thank Raymond Plaut and Tian Yu for their useful comments and discussions on *elastica* and thank Mingwu Li for the discussions on COCO.

References

- [1] Reddy, J. N. [2014] *An Introduction to Nonlinear Finite Element Analysis: with applications to heat transfer, fluid mechanics, and solid mechanics*. OUP Oxford.
- [2] Bert, C. W. and Malik, M. [1996] Differential quadrature method in computational mechanics: a review. *Applied Mechanics Reviews* **49**(1):1–28.
- [3] Liu, G.-R. [2009] *Meshfree methods: moving beyond the finite element method*. Taylor & Francis.
- [4] Koon, W. S., Lo, M. W., Marsden, J. E. and Ross, S. D. [2011] *Dynamical Systems, the Three-Body Problem and Space Mission Design*. Marsden Books, ISBN 978-0-615-24095-4.
- [5] Xu, M. and Xu, S. [2007] J_2 invariant relative orbits via differential correction algorithm. *Acta Mechanica Sinica* **23**(5):585–595.
- [6] Breakwell, J. V. and Brown, J. V. [1979] The ‘halo’ family of 3-dimensional periodic orbits in the Earth-Moon restricted 3-body problem. *Celestial Mechanics* **20**(4):389–404.
- [7] Mains, D. [1993] *Transfer trajectories from Earth parking orbits to L1 halo orbits*. Ph.D. thesis, Master’s thesis, Department of Aeronautics and Astronautics, Purdue
- [8] Barden, B. T. [1994] Using stable manifolds to generate transfers in the circular restricted problem of three bodies. *Master degree thesis. West Lafayette: School of Aeronautics and Astronautics, Purdue University* .
- [9] Parker, T. S. and Chua, L. [2012] *Practical numerical algorithms for chaotic systems*. Springer Science & Business Media.
- [10] Naik, S. and Ross, S. D. [2017] Geometry of escaping dynamics in nonlinear ship motion. *Communications in Nonlinear Science and Numerical Simulation* **47**:48 – 70.
- [11] Ross, S. D., BozorgMagham, A. E., Naik, S. and Virgin, L. N. [2018] Experimental validation of phase space conduits of transition between potential wells. *Physical Review E* **98**(5):052214.
- [12] Naik, S., García-Garrido, V. J. and Wiggins, S. [2019] Finding NHIM: Identifying high dimensional phase space structures in reaction dynamics using Lagrangian descriptors. *Communications in Nonlinear Science and Numerical Simulation* **79**:104907.
- [13] Sundararajan, P. and Noah, S. [1997] Dynamics of forced nonlinear systems using shooting/arc-length continuation method—application to rotor systems. *Journal of Vibration and Acoustics* **119**(1):9–20.

- [14] Liu, F. and Zhou, J. [2018] Shooting and arc-length continuation method for periodic solution and bifurcation of nonlinear oscillation of viscoelastic dielectric elastomers. *Journal of Applied Mechanics* **85**(1):011005.
- [15] Zhong, J., Fu, Y., Chen, Y. and Li, Y. [2016] Analysis of nonlinear dynamic responses for functionally graded beams resting on tensionless elastic foundation under thermal shock. *Composite Structures* **142**:272–277.
- [16] Sabir, A. and Djoudi, M. [1995] Shallow shell finite element for the large deflection geometrically nonlinear analysis of shells and plates. *Thin-walled structures* **21**(3):253–267.
- [17] Zhong, J., Virgin, L. N. and Ross, S. D. [2018] A tube dynamics perspective governing stability transitions: An example based on snap-through buckling. *International Journal of Mechanical Sciences* **149**:413–428.
- [18] Zhong, J. and Ross, S. D. [2019] Geometry of escape and transition dynamics in the presence of dissipative and gyroscopic forces in two degree of freedom systems. *Communications in Nonlinear Science and Numerical Simulation* 105033.
- [19] Crisfield, M. A. [1981] A fast incremental/iterative solution procedure that handles “snap-through”. In *Computational Methods in Nonlinear Structural and Solid Mechanics*, 55–62. Elsevier.
- [20] Riks, E. [1979] An incremental approach to the solution of snapping and buckling problems. *International Journal of Solids and Structures* **15**(7):529–551.
- [21] Dankowicz, H. and Schilder, F. [2013] *Recipes for continuation*. SIAM.
- [22] De Borst, R., Crisfield, M. A., Remmers, J. J. and Verhoosel, C. V. [2012] *Nonlinear finite element analysis of solids and structures*. John Wiley & Sons.
- [23] Fafard, M. and Massicotte, B. [1993] Geometrical interpretation of the arc-length method. *Computers & Structures* **46**(4):603–615.
- [24] Plaut, R. and Virgin, L. [2009] Vibration and snap-through of bent elastica strips subjected to end rotations. *Journal of Applied Mechanics* **76**(4):041011.
- [25] Virgin, L. N. [2007] *Vibration of axially-loaded structures*. Cambridge University Press.
- [26] Seydel, R. [2009] *Practical bifurcation and stability analysis*. Springer Science & Business Media.
- [27] Krauskopf, B., Osinga, H. M. and Galán-Vioque, J. [2007] *Numerical continuation methods for dynamical systems*. Springer.
- [28] Kreja, I. and Schmidt, R. [2006] Large rotations in first-order shear deformation FE analysis of laminated shells. *International Journal of Non-Linear Mechanics* **41**(1):101–123.

- [29] Fujii, F. [1989] Scheme for elasticas with snap-back and looping. *Journal of Engineering Mechanics* **115**(10):2166–2181.
- [30] Han, S.-C., Ham, H.-D. and Kanok-Nukulchai, W. [2008] Geometrically non-linear analysis of arbitrary elastic supported plates and shells using an element-based Lagrangian shell element. *International Journal of Non-Linear Mechanics* **43**(1):53–64.
- [31] DaDeppo, D. and Schmidt, R. [1975] Instability of clamped-hinged circular arches subjected to a point load. *Journal of Applied Mechanics* **42**(4):894–896.
- [32] Lanzo, A. D. [2009] Nonlinear analysis of elastic high-shear deformable plane frames by a mixed FEM path-following approach. *International Journal of Solids and Structures* **46**(7-8):1764–1771.
- [33] Nukala, P. K. V. and White, D. W. [2004] A mixed finite element for three-dimensional nonlinear analysis of steel frames. *Computer Methods in Applied Mechanics and Engineering* **193**(23-26):2507–2545.
- [34] Simo, J. C. and Vu-Quoc, L. [1986] A three-dimensional finite-strain rod model. Part II: Computational aspects. *Computer Methods in Applied Mechanics and Engineering* **58**(1):79–116.
- [35] Kapania, R. and Li, J. [2003] A formulation and implementation of geometrically exact curved beam elements incorporating finite strains and finite rotations. *Computational Mechanics* **30**(5-6):444–459.
- [36] Živković, M., Kojić, M., Slavković, R. and Grujović, N. [2001] A general beam finite element with deformable cross-section. *Computer Methods in Applied Mechanics and Engineering* **190**(20-21):2651–2680.
- [37] Gerstmayr, J. and Irschik, H. [2008] On the correct representation of bending and axial deformation in the absolute nodal coordinate formulation with an elastic line approach. *Journal of Sound and Vibration* **318**(3):461–487.
- [38] Yang, Y.-B. and Shieh, M.-S. [1990] Solution method for nonlinear problems with multiple critical points. *AIAA journal* **28**(12):2110–2116.
- [39] Yang, Y., Lin, S. and Leu, L. [2007] Solution strategy and rigid element for nonlinear analysis of elastically structures based on updated Lagrangian formulation. *Engineering Structures* **29**(6):1189–1200.
- [40] Virgin, L., Wiebe, R., Spottswood, S. and Eason, T. [2014] Sensitivity in the structural behavior of shallow arches. *International Journal of Non-Linear Mechanics* **58**:212–221.
- [41] Harvey Jr, P. and Virgin, L. [2015] Coexisting equilibria and stability of a shallow arch: Unilateral displacement-control experiments and theory. *International Journal of Solids and Structures* **54**:1–11.

- [42] Rhim, J. and Lee, S. W. [1998] A vectorial approach to computational modelling of beams undergoing finite rotations. *International Journal for Numerical Methods in Engineering* **41**(3):527–540.
- [43] Pi, Y.-L. and Bradford, M. A. [2012] Non-linear in-plane analysis and buckling of pinned–fixed shallow arches subjected to a central concentrated load. *International Journal of Non-Linear Mechanics* **47**(4):118–131.
- [44] Pandey, A., Moulton, D. E., Vella, D. and Holmes, D. P. [2014] Dynamics of snapping beams and jumping poppers. *Europhysics Letters* **105**(2):24001.
- [45] Li, Z. [2007] A mixed co-rotational formulation of 2D beam element using vectorial rotational variables. *Communications in Numerical Methods in Engineering* **23**(1):45–69.
- [46] Harrison, H. B. [1978] Post-buckling behaviour of elastic circular arches. *Proceedings of the Institution of Civil Engineers* **65**(2):283–298.
- [47] Hashemian, A. and Hosseini, S. F. [2019] Nonlinear bifurcation analysis of statically loaded free-form curved beams using isogeometric framework and pseudo-arclength continuation. *International Journal of Non-Linear Mechanics* **113**:1–16.
- [48] Lacarbonara, W. [2013] *Nonlinear structural mechanics: theory, dynamical phenomena and modeling*. Springer Science & Business Media.
- [49] Fu, Y., Zhong, J. and Chen, Y. [2014] Thermal postbuckling analysis of fiber–metal laminated plates including interfacial damage. *Composites Part B: Engineering* **56**:358–364.
- [50] Luu, A.-T. and Lee, J. [2016] Non-linear buckling of elliptical curved beams. *International Journal of Non-Linear Mechanics* **82**:132–143.
- [51] Fu, Y.-M. [2013] *Nonlinear analyses of laminated plates and shells with damage*. WIT Press.
- [52] Striz, A. G., Jang, S. K. and Bert, C. W. [1988] Nonlinear bending analysis of thin circular plates by differential quadrature. *Thin-Walled Structures* **6**(1):51–62.
- [53] Thurston, G. A. [1961] A numerical solution of the nonlinear equations for axisymmetric bending of shallow spherical shells. *Journal of Applied Mechanics* **28**(4):557–562.
- [54] Dumir, P. [1985] Nonlinear axisymmetric response of orthotropic thin spherical caps on elastic foundations. *International Journal of Mechanical Sciences* **27**(11-12):751–760.
- [55] Boroujerdy, M. S. and Eslami, M. [2014] Axisymmetric snap-through behavior of Piezo-FGM shallow clamped spherical shells under thermo-electro-mechanical loading. *International Journal of Pressure Vessels and Piping* **120**:19–26.